Laser-excited Mach cones in a dusty plasma crystal

A. Melzer,* S. Nunomura,[†] D. Samsonov,[‡] Z. W. Ma, and J. Goree[§]

Department of Physics and Astronomy, The University of Iowa, Iowa City, Iowa 52242

(Received 31 March 2000)

Experimental studies of the formation and structure of Mach cones in a plasma crystal are presented. Plasma crystals are ordered structures of charged microspheres trapped in the sheath of an rf discharge plasma. Using a monolayer crystal with a hexagonal lattice, Mach cones were excited by the radiation pressure of a focused laser beam. The beam was swept at a supersonic speed through the crystal, in a controlled and repeatable manner. A multiple Mach cone structure was observed, with at least three distinct Mach cones. The Mach angle relation was verified over a wide range of Mach numbers, for both the first and second cones. The sound speed, measured from the first Mach angle, was found to increase with the particle number density. Two methods of determining the particle charge and screening distance are developed, making use of the sound speed and an assumption of a Yukawa interparticle potential. Molecular-dynamics simulations of the experiment were carried out, using a monolayer of particles interacting through a Yukawa potential, and these show close agreement with the experiment.

PACS number(s): 52.25.Zb, 47.40.−x

I. INTRODUCTION

A dusty plasma is an ionized gas containing a suspension of small particles of solid matter. These particles are in general micron-sized, and they are often called ''dust.'' They acquire a large electric charge by collecting free electrons and ions from the plasma. Dusty plasmas occur naturally, for example in interstellar space and Saturn's rings [1]. In the laboratory, dusty plasmas are made either by introducing manufactured particles into a plasma, or by growing the particles in the gas phase by nucleation and aggregation.

In the laboratory it is possible to trap micron-sized particles in a stable equilibrium provided by electrostatic forces and gravity. An additional force acting on the particles is damping on the ambient neutral gas. This damping reduces the particles' random kinetic energy below the interparticle potential energy. Under these circumstances, the dusty plasma is said to be ''strongly coupled,'' and the particles arrange themselves in an ordered pattern, or Coulomb lattice [2–6]. This lattice can be in a gas, liquid, or solid phase, depending on the particle size and discharge operating parameters [7,8]. To describe these strongly coupled dusty plasmas, various authors have used the terms ''plasma crystals,'' ''colloidal plasmas,'' and ''complex plasmas,'' where the latter two terms are analogies to the condensed matter fields of colloidal suspensions and complex fluids.

When the plasma is generated by a high voltage on a horizontal electrode, the lattice generally forms in horizontal layers in the sheath above the electrode. Depending on the

apparatus and particle size, there can be a single layer or as many as several tens of layers.

Experiments have shown that in the horizontal direction, the force between two particles is modeled accurately by a Yukawa potential [9]. The interparticle force in the vertical direction is more complicated due to the presence of an ion focus downstream of particles exposed to an ion flow [10,11]. This complication is avoided when the experiment is operated with a single horizontal layer. Such an experiment is two-dimensional (2D) and is well suited for comparison to molecular-dynamics (MD) simulations parametrized by the charge Q, Debye length λ_D, and interparticle spacing a. It is common to describe the shielding length and the particle spacing by the dimensionless quantity $\kappa \equiv a/\lambda_D$. The particle spacing is determined partly by the geometry of the external confining potential, which is provided by the bowl-shaped curvature of the sheath that levitates the particles.

The lattice sustains compressional waves, and when it is in a solid phase it also sustains transverse shear waves. In seismology these are termed the P and S waves, respectively. In dusty plasmas, the compressional wave is sometimes called the dust lattice wave (DLW). For long wavelengths, i.e., small values of the wave number q, the dispersion relations of both the compressional and transverse wave are acoustic, $\omega \propto q$, if the interparticle potential is Yukawa.

There are several ways these waves can be excited; here we will make use of the laser-excitation method of Homann et al. [12,13]. They launched compressional waves in 1D and 2D plasma crystals using a laser beam focused on the dust particles. In this method of wave excitation, photons are reflected or absorbed by the particle, imparting a momentum to the particle in the direction of the laser beam. There may be additional forces on the particles, such as a gas-phase force due to heating the particle surface. In any case, regardless of the mechanisms involved in the force, it has been established empirically that a laser beam can apply a strong force to the particles and move them in the direction of the beam. Homann et al. modulated the laser intensity by chopping it, causing a compressional DLW to be excited in a plasma

(a)

(b)

galvanometer
scanning
mirror

Ar laser
beam

(c)

chamber
wall

ring
upper
electrode

micro-
spheres

Ar laser
beam

probe

lower
electrode

glass
vacuum
window

2 cm

(d)

scope   func
gen   servo
amp

frame
grabber

video camera
(top view)

micro lens

galvanometer
scanning
mirror

HeNe laser
horizontal
sheet

Ar laser
beam

RF

lower electrode   microspheres
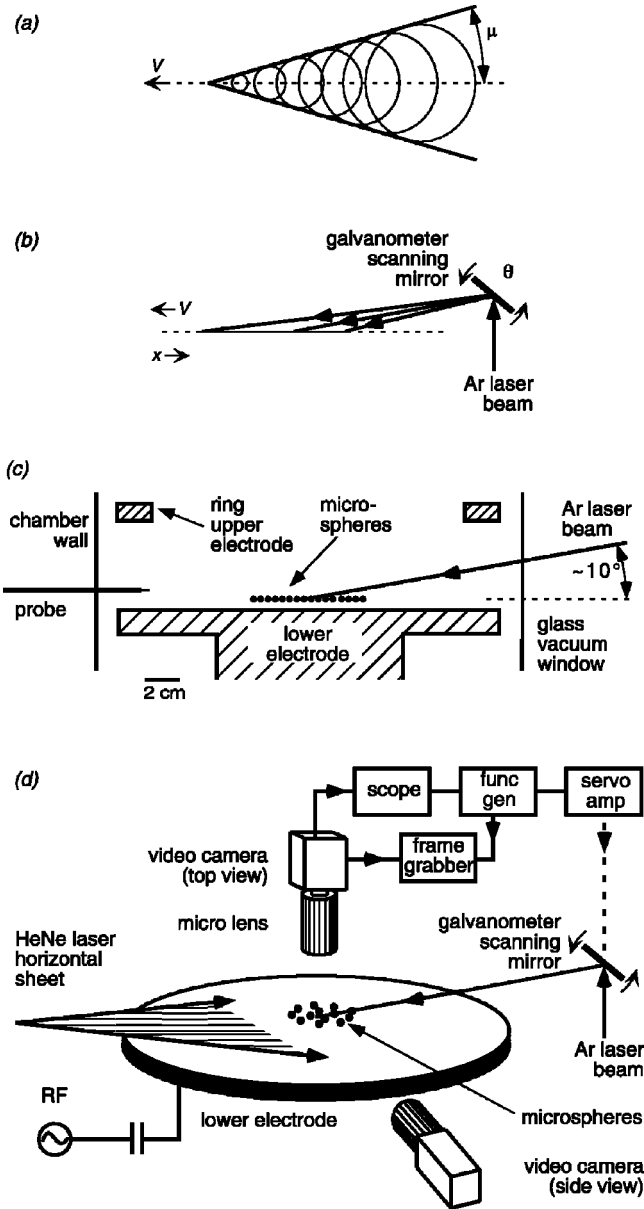
video camera
(side view)

FIG. 1. Method of generating Mach cones. (a) A supersonic disturbance moving to the left at velocity V produces circular wavefronts, which superimpose to create a cone with a half-angle μ. (b) An argon laser beam is steered by a galvanometer scanning mirror, which rotates at fixed angular velocity, thereby moving a laser spot at velocity V in the $-\hat{x}$ direction. The laser beam applies a force to the microspheres in the $-\hat{x}$ direction. (c) Scale drawing of the electrode and vacuum chamber. Microspheres are levitated in a plasma, 9 mm above a capacitively coupled rf electrode. (d) Sketch of viewing and triggering setup. A low-power horizontal laser sheet illuminates the monolayer of particles for both the top and side view cameras. An oscillator in the top camera triggers an oscilloscope, which is used as a pulse generator to trigger an arbitrary function generator. The latter drives the scanning mirror.

crystal. Here, we will adapt this laser excitation technique to produce Mach cones.

When acoustic waves are excited by the movement of a supersonic object, they form a series of circular wavefronts, which superimpose to form a Mach cone, as sketched in Fig. 1(a). The geometry of the superposition determines the Mach

angle μ, according to

$$1/\sin\mu = M, \tag{1}$$

where $M \equiv V/c$. Here V is the velocity of the supersonic perturbation and c is the acoustic speed in the undisturbed medium. Testing Eq. (1) is one of the purposes of this paper.

The existence of Mach cones in dusty plasmas was originally predicted by Havnes et al. [1,14]. They suggested that Mach cones are produced in the layers of dust in Saturn's rings. This dust is charged by exposure to the Saturnian magnetospheric plasma. Charged dust particles rotate about the planetary axis at the same angular velocity as the planet itself, whereas boulders move in Keplerian orbits at a different speed. The difference in their speeds is supersonic, compared to the sound speed in the charged dust. It is anticipated that when the Cassini spacecraft arrives at Saturn in 2004, its cameras might possibly be able to image Mach cones in the rings. Havnes et al. presented calculations that predict the conditions where the cones are likely to occur.

Mach cones are most familiar in the field of gas dynamics [15]. Less commonly, they also occur in solid matter [16]. They should not be confused with ship's wakes, which, due to their nonacoustic dispersion, have a cone angle that is independent of the speed of the ship [17].

Using simulations, the dispersion relations of compressional and transverse (shear) waves in a 2D Yukawa system were computed by Peeters and Wu [18], in the absence of damping. They found that both waves are dispersionless, i.e., acoustic at long wavelengths. The speed of these two acoustic waves was found to depend on the screening strength κ. They also found that the compressional wave is faster than the transverse wave by a factor of typically 5, for $\kappa = 1$.

The sound speed for the compressional wave in a 2D Yukawa system, in the absence of damping and thermal effects, can be written as

$$c = c_0 f(\kappa), \tag{2}$$

where

$$c_0 \equiv \sqrt{\frac{Q^2}{4\pi\epsilon_0 ma}}$$

is a natural unit of the sound velocity, m is the particle mass, and the second term

$$f(\kappa) = \sqrt{\sum_{\vec{r}_a} \frac{1}{r_a}\exp(-r_a\kappa)\left[\frac{15}{8}(1+r_a\kappa)+\frac{9}{8}r_a^2\kappa^2\right]} \tag{3}$$

depends only on the screening strength κ. Here, the sum is over all possible translation vectors $\vec{r}_a$ in a hexagonal lattice, and $r_a = |\vec{r}_a|$ is normalized to the particle separation a. The behavior of the function f is shown in Fig. 11. One should note that c_0 is not the sound velocity for the Coulomb case $\kappa = 0$. In fact, as $\kappa \to 0$ the compressional wave becomes nonacoustic with $\omega \propto \sqrt{q}$.

This expression for the sound speed of the compressional wave is derived assuming a springlike interaction between the particles in the Yukawa system where the spring constant is given by the second derivative of the Yukawa potential.

The coefficients 15/8 and 9/8, rather than 2 and 1 as in the usual 1D treatment [19], follow from the hexagonal crystal structure.

Samsonov *et al.* [20,21] detected Mach cones in a laboratory dusty plasma using a crystalline hexagonal monolayer of microspheres suspended in the sheath of an rf plasma. Beneath the monolayer, which was stable, there were a few unstable particles that moved horizontally at a speed of several cm/s. Because these unstable particles were charged, they disturbed the main layer above them. Samsonov *et al.* imaged the particles in the monolayer using a video camera, and from the digitized images they produced maps of the particle velocity. These maps showed V-shaped disturbances that were identified as Mach cones. Samsonov *et al.* carried out a test of Eq. (1), and verified that it was obeyed, within the error bars, for the range of supersonic velocities V that were observed. In the experiment they found not just one V-shaped cone, as in a gas, but two cones. The first was compressive, with particles pushed in the forward direction, and the second was rarefactive, with particles moving back toward their original positions. The existence of the second cone was attributed to the restoring force of the interparticle bonds in a solid state. Molecular-dynamics simulations carried out with a Yukawa interparticle potential revealed not only the second cone, but additional cones as well, as particles oscillated around their equilibrium lattice positions following the passage of the initial disturbance. The experimenters were unable to detect the presence of a third cone, presumably because it was too weak to be detected using their method. An analysis of the interparticle bonds showed that the particle motion was primarily elastic, rather than plastic, meaning that lattice defects were not generated. Smoothing their particle image data, they produced profiles of continuum parameters, such as particle number density, which allowed them to analyze the Mach cone disturbance using methods familiar in shock physics.

In this paper, we report experiments similar to those of Samsonov *et al.* [20,21]. Here, however, we used an argon laser beam, which we focused onto a spot on the lattice plane, in the manner of Homann *et al.* [12,13]. To excite a Mach cone, we moved the laser spot across the crystalline lattice at a velocity V of several cm/s, which is faster than the acoustic speed of the compressional wave. We did this by bouncing the beam from a rotatable scanning mirror, as shown in Fig. 1(b). This method has the advantage that the timing and velocity of the supersonic disturbance are controlled, allowing us to make measurements over a wide range of V and to repeat them many times. Each scan was identical, except for the initial particle positions within the lattice. By averaging over 100 scans, we were able to reduce the noise in our images.

We also carried out molecular dynamics (MD) simulations of the experiment. Using a Yukawa potential and applying a force like that of the moving laser spot, and including the effects of damping, we found results very similar to the experiment.

II. APPARATUS

The experiments were performed in a capacitively coupled radio-frequency plasma. A cross-sectional view of

TABLE I. Discharge parameters and measured crystal properties, for six different experimental conditions. Here, V_{rf} is indicated as a peak-to-peak voltage. Experiments I–III all had the same plasma conditions.

| Parameter | Units | Experiment number | | | | | |
		I	II	III	IV	V	VI
Discharge conditions							
V_{rf}	V	52	52	52	150	134	176
$-V_{bias}$	V	33	33	33	136	116	103
P	W	5	5	5	25	20	30
Plasma parameters in bulk plasma							
V_{pl}	V		20.7		21.9	21.9	21.6
T_e	eV		1.86		2.01	2.01	1.79
n_e	10^9 cm^{-3}		1.1		5.1	5.0	3.4
λ_D	μm		307		148	149	170
Particle measurements							
a	μm	611.6	802.7	557.0	371.7	418.9	463.0
c	mm/s	27.7	20.5	26.4	24.0	22.6	19.9

our experimental apparatus is shown in Fig. 1(c). We used the same electrodes and vacuum chamber as Samsonov *et al.* [20,21]. The main difference, however, is that we used an argon-ion laser to excite the Mach cones.

The argon laser was focused with a telescope. At its focus in the vacuum chamber, the beam had a Gaussian fullwidth at halfmaximum (FWHM) of 0.5 mm. In this paper we will report the laser power measured at the output of the laser, which had a maximum of 1.6 W. In the sample region inside the vacuum chamber, the laser power was measured to be reduced by approximately 50% due to losses at the mirrors and windows.

The beam was incident on the plasma crystal above the lower electrode at a grazing angle of approximately 10°, as shown Fig. 1(c). This angle was varied by a galvanometer laser scanner, i.e., a mirror that is turned by a servo. By ramping the servo voltage linearly, the mirror was rotated at a constant angular velocity, so that the beam moved across the electrode at a speed V that was constant, to within 5%, over the camera's field of view. The apparatus allows a wide range of V. We operated with an angular velocity in the range from 0.3 to 1.5 s^{-1}, corresponding to $14 \leqslant V \leqslant 94$ mm/s.

An argon plasma was generated by applying different rf voltages between 50 and 180 V at 13.56 MHz to the horizontal lower electrode through an impedance matching network. The input power ranged from 5 to 30 W. The gas pressure was regulated at 10 mtorr (13 Pa) using a gas flow rate of 0.5 sccm. Operating at such a low pressure provided a low level of damping of particles by the neutral gas. The plasma parameters, measured with a Langmuir probe inserted 16 mm above the lower electrode, were $T_e \approx 2$ eV and $n_e = (1-5) \times 10^9$ cm^{-3}. The dc self-bias on the lower electrode was -33 to -136 V. This bias helped provide the vertical dc electric field that levitated the particles. A summary of the different discharge conditions is given in Table I.

A dusty plasma crystal was formed by shaking monodisperse particles into the plasma. The particles were polymer spheres of 6.5 ± 0.3 μm in diameter, with a mass density of 1514 kg/m^3 corresponding to a particle mass of $m = 2.18 \times 10^{-13}$ kg. After they were dispersed into the plasma, the particles became negatively charged. They were trapped in a monolayer crystal with a diameter of approximately 5 cm. Particles were levitated in the electrode sheath at a height 9 mm above the electrode. The particles arranged into a hexagonal lattice, with an interparticle spacing that was nonuniform over the whole dust cloud. Under the same plasma conditions of experiment I, II, and III (see Table I), the particle spacing ranged from 557 to 802 μm. The particles were spaced more closely near the center of the cloud, due to the weight of the particles uphill on the sides of the bowl-like radial confining potential [22,23].

The particles were imaged by illumination with a horizontal He-Ne laser sheet. They were viewed through the top window by a video camera using a 632.8 nm interference filter. The field of view was 24×18 mm, and it included 700–3500 particles. The images were digitized with an eight-bit gray scale and a 640×480 pixel resolution.

For each laser scan, two consecutive frames, separated by 33 ms, were recorded on a PC. The frames were synchronized to the motion of the laser beam so that the video always captured the passage of the Mach cone at the same time and position. This was done using the triggering scheme shown in the upper part of Fig. 1(d). The video camera served as the master oscillator. The first vertical-line signal in the camera's output waveform was used to trigger an oscilloscope, which was not used to view the waveform, but merely as a convenient generator of a single pulse. The repetition rate of the trigger pulse was reduced from the 30 Hz video rate to a much slower rate in the range 0.3–1 Hz. This allowed the crystal sufficient time to anneal after the disturbance created by the previous laser scan.

The oscilloscope pulse triggered two events: the beginning of the waveform that moved the galvanometer scanning mirror, and, after a delay adjusted to the scanning speed of the mirror, the grabbing of the two video frames. Taking advantage of the repeatability of the timing in this triggering scheme, we averaged our images of the Mach cones over 100 laser scans, all under the same conditions. This averaging provided an improved signal-to-noise ratio, allowing us to image features that were previously undetectable, such as the third Mach cone.

As a test of linearity, we repeated experiments at seven laser power levels ranging from 0.2 to 1.6 W. The results appear to rule out the possibility of strong nonlinear effects, but are inconclusive in assessing the presence of weak nonlinearity. The angle of the first Mach cone may have increased from 46° at 0.2 W to 51° at 1.6 W. However, because of the error-bar size in this measurement, it is also possible that the angle did not change at all. Thus, our test suggests a slight nonlinearity, but they are not conclusive. A more powerful laser or a more sensitive measurement would be required to make a definitive identification of nonlinearity.

Besides the improvement of the Mach cone imaging, our choice of a laser instead of a moving charged particle as the supersonic object resulted in a fundamental difference in the
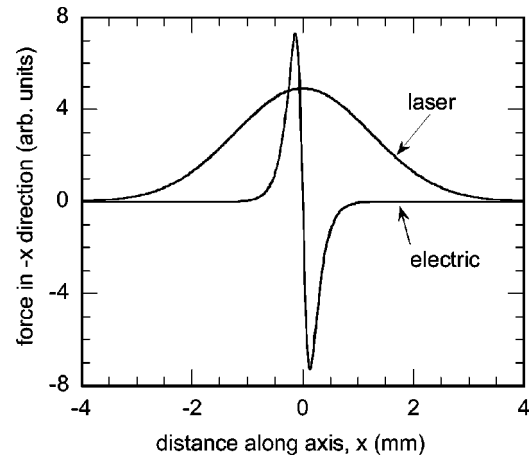

FIG. 2. Comparison of forces acting on particles in the monolayer. Shown here is the component of force in the forward $(-\hat{x})$ direction, as a function of x, where the latter is equivalent to time, $x = Vt$. For excitation by a moving charged particle located in a plane 0.2 mm below the monolayer, the force on a particle in the lattice reverses direction as the moving particle goes by. The Debye length, which was assumed here to be 0.35 mm, limits the range of the electric force. The optical force, on the other hand, is always in the forward direction, and it is spread over several millimeters in the $-\hat{x}$ direction due to the 10° angle of the laser beam. The optical force is applied to a more compact region in the $\hat{y}$ direction, not shown here. This figure is intended to illustrate the direction of the force; the spatial distribution on the horizontal axis is drawn to scale, but the vertical axis has an arbitrary scale. The magnitudes of the electric and optical forces depend on the particle charge and laser power, respectively, and therefore they are not drawn here to the same scale.

forces acting on a particle. Figure 2 shows a comparison of the forces acting on a particle from the focused laser beam and the moving charged particle of the experiments of Ref. [20]. Due to the small inclination of the laser beam, the radiation pressure provides a force which always pushes the particles forward, i.e., in the direction of the laser beam. The charged particle and its Debye cloud, however, move below the crystal layer. Therefore, a crystal-layer particle is first pushed in the forward direction, and when the moving charged particle has passed the crystal particle, it is pushed backwards. That means that the mean force on a crystal particle is zero in the case of the supersonic lower-layer particles. The laser, however, provides a net momentum $\int F_L dt$ in the forward direction.

III. IMAGES OF MACH CONES

A. Mach cone maps

The Mach cone experiments were performed in a single-layer lattice that was highly ordered. Figure 3 shows the pair correlation function and the orientational correlation function for a typical crystal under the conditions of experiment V (see Table I). The pair correlation function exhibits a large number of peaks, indicating a long-range translational order. The orientational correlation has a correlation length of about 5500 μm, which is 13 times the interparticle distance of $a = 419$ μm; this large multiple reflects a high orientational ordering. Crystals with such a high order are possible
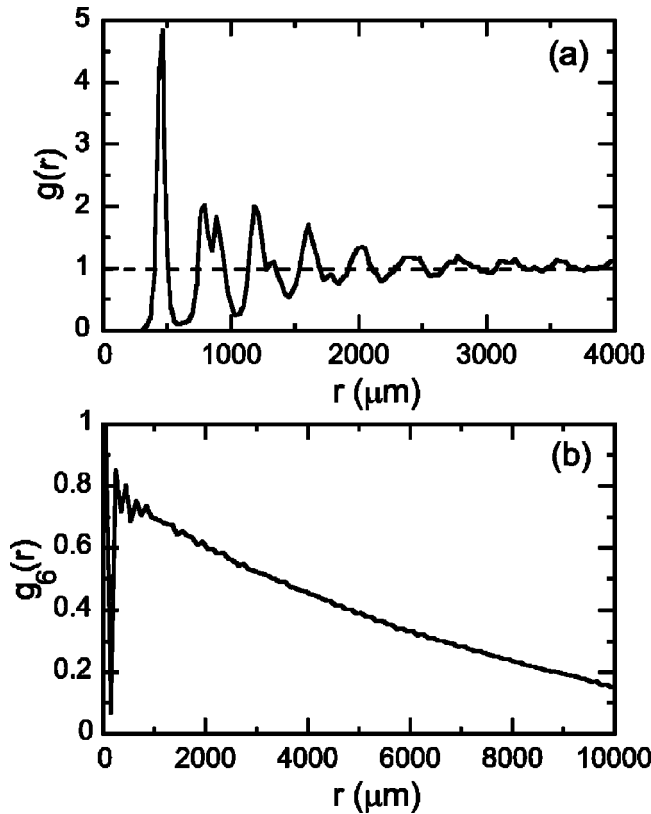
FIG. 3. (a) Pair correlation function $g(r)$ and (b) orientational correlation function $g_6(r)$ for a typical monolayer crystal, in which the Mach cones are studied. These correlations indicate a high degree of order.
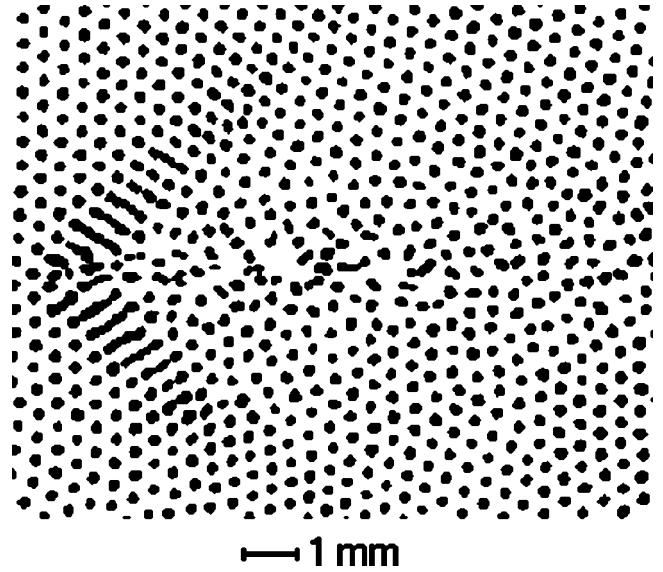

FIG. 4. Single video frame with a Mach cone. The image has been thresholded and inverted, so that particles appear as black spots. When measuring the particle (x,y) coordinates, we computed the center of these spots, weighted by the pixel intensity, yielding a subpixel resolution.

at these low gas pressures only when arranged in a single layer. With more layers, they are unstable due to ion streaming [24,25]. Note that the video images of particles that we used in computing the correlation functions were disturbed by the presence of a Mach cone structure; the undisturbed medium probably had a slightly higher order than shown in Fig. 3.

The analysis of the Mach cones starts from the digitized gray-scale video images. As usual, the particle (x,y) coordinates are found by computing the center of a particle. Particles are identified by pixels that are brighter than a threshold level. Contiguous bright pixels are treated as a single particle, and their center is found, weighting it by the intensity of each pixel. This method provides subpixel spatial resolution. The particle velocity $\vec{v}$ (not to be confused with the speed of the laser spot V) is determined by tracking a particle from one video frame to the next.

Figure 4 shows an example of a video image. The image shown has been thresholded and inverted, so that it appears in black and white. Here the laser spot moved from right to left, producing a Mach cone that in this example can be easily identified. More often, however, the cones are difficult to identify in the raw video image because the particles are displaced by only small distances from their equilibrium positions. For this reason, we rely on images that have been processed in other ways.

Maps of the particle speed $|\vec{v}|$ in Fig. 5 reveal the Mach cone structure in the crystal. These images are less noisy than in previous experiments [20,21], because we averaged

100 repeatable events. In Fig. 5, speed maps are shown for laser velocities ranging from 17.6 to 93.6 mm/s. The discharge conditions are those of experiment V in Table I. At the lowest laser speed, no Mach cone is visible, but all others show a clear Mach cone structure. As expected, with increasing (supersonic) laser velocity V, the Mach cones become narrower and narrower. In most cases, at least two cones are observable, and for $V=23.4$ mm/s and $V=29.3$ mm/s even a third cone can be identified. We will discuss the third cone further in Sec. III B.

We devised an additional method to visualize the Mach cone structure that is similar to the method of Schlieren photography in gas dynamics. To explain our method, we first review how Schlieren photography works. A transparent gaseous medium is homogeneously illuminated by a pointlike light source. Density changes in the medium, e.g., due to a shock, modulate the corresponding refractive index. The light is diffracted in these regions, giving rise to the appearance of streaks in the otherwise homogeneous illumination. The term ''Schlieren'' means ''streaks'' in German.

Our method yields what we call ''numerical Schlieren maps,'' which are analogous to Schlieren photographs. Our maps correspond roughly to a snapshot of the time derivative of the particle number density. We begin with the original gray-scale inverted video images, which have dark particles on a light background. To reduce graininess, we average 100 images for each video frame. This averaging process takes advantage of the random particle movement between scans, so that particles are in slightly different positions in each of the 100 images. The averaged images correspond roughly to number density maps. To emphasize the small difference in number density produced by the Mach cone, we compute the difference in the pixel intensities of two consecutive frames. This yields our numerical Schlieren map. It has the advantage that it requires less effort to prepare than speed maps,
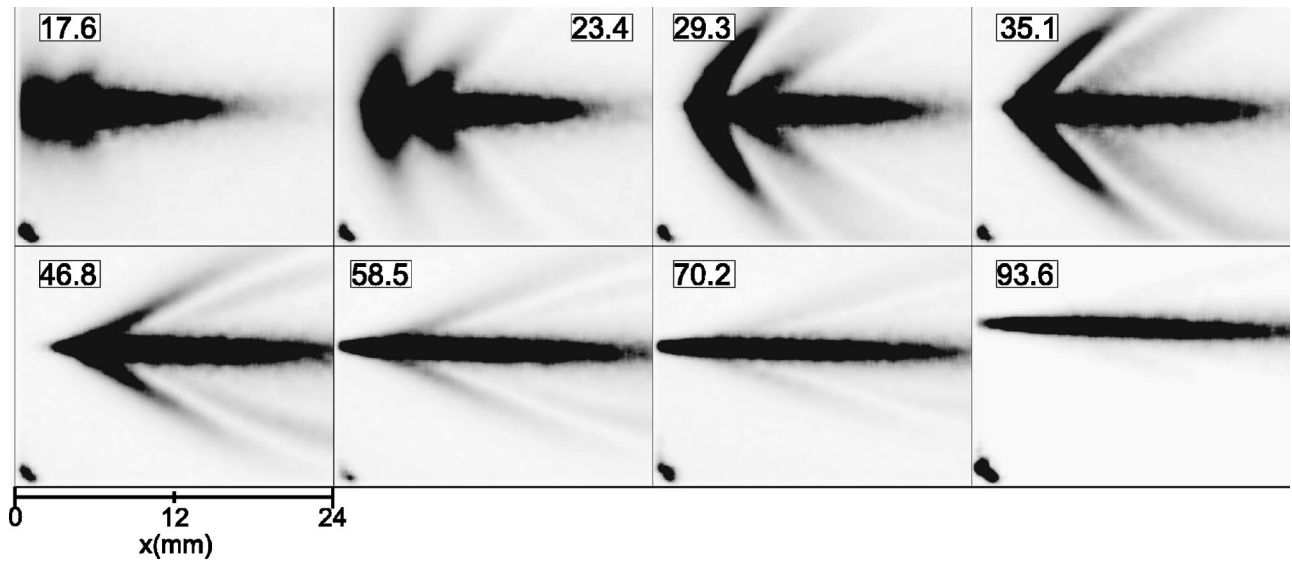
FIG. 5. Gray-scale maps of the particle speed $v = |\vec{v}|$ for different speeds of the laser spot V. Dark gray values correspond to high particle velocities (black corresponds to $v \geq 4$ mm/s). The numbers in the boxes indicate the laser speed in mm/s. The dark spot in the lower-left corner is an artifact, and it is unrelated to the Mach cones. The experimental conditions were those of experiment V in Table I.

although they are noisier since they are obtained from a small difference in pixel gray values.

Our numerical Schlieren maps in Fig. 6 clearly reveal the cone structure. These maps were prepared under the same conditions as the speed maps in Fig. 5. Comparing the Schlieren and speed maps, we note that the Mach cone angles do not exactly match. We will rely on the Mach cone angles measured from the speed maps, since they represent an actual physical parameter.

Hereafter, we will focus our attention on maps corresponding to a laser spot velocity of 29.3 mm/s. In this case, the Mach number is $M = 1.3$, based on the angle of the first Mach cone in the speed map of Fig. 5. A wiremesh version of the speed map, Fig. 7(a), offers perhaps the clearest evidence that there is not only a first and second cone, but a third cone as well.

While only two cones were seen in previous experiments [20,21], we observed three, verifying the prediction of simulations [20]. Our observation of a third cone also rules out the possibility that the two previously observed cones might correspond to the two different wave modes, compressional and shear, that can propagate in a crystalline lattice. The cone angles measured from Fig 5 are $\mu_1 = 53°$, $\mu_2 = 41.5°$, and $\mu_3 = 28.9°$ for the first, second and third cones, respectively. The ''amplitude'' of the third cone is much weaker than that of the first and second, for reasons that we will discuss in Sec. V.

In conclusion, we have shown that Mach cones can be excited by using the radiation pressure of a focused laser beam that is moved with supersonic speed through the crystal. As in the experiments of Homann et al. [12,13], the laser excited compressional waves in the lattice, and because of the supersonic excitation, these waves superimpose to form the expected Mach cone. The existence of more than two cones was verified.
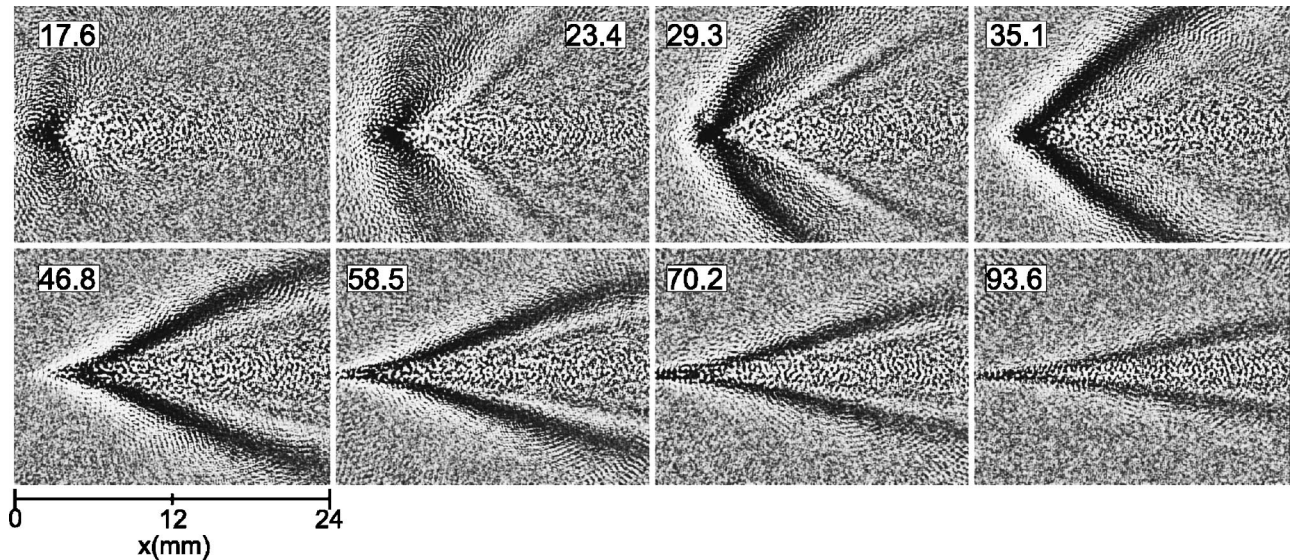

FIG. 6. Numerical Schlieren maps with different speeds of the laser spot V for the same data as Fig. 5.
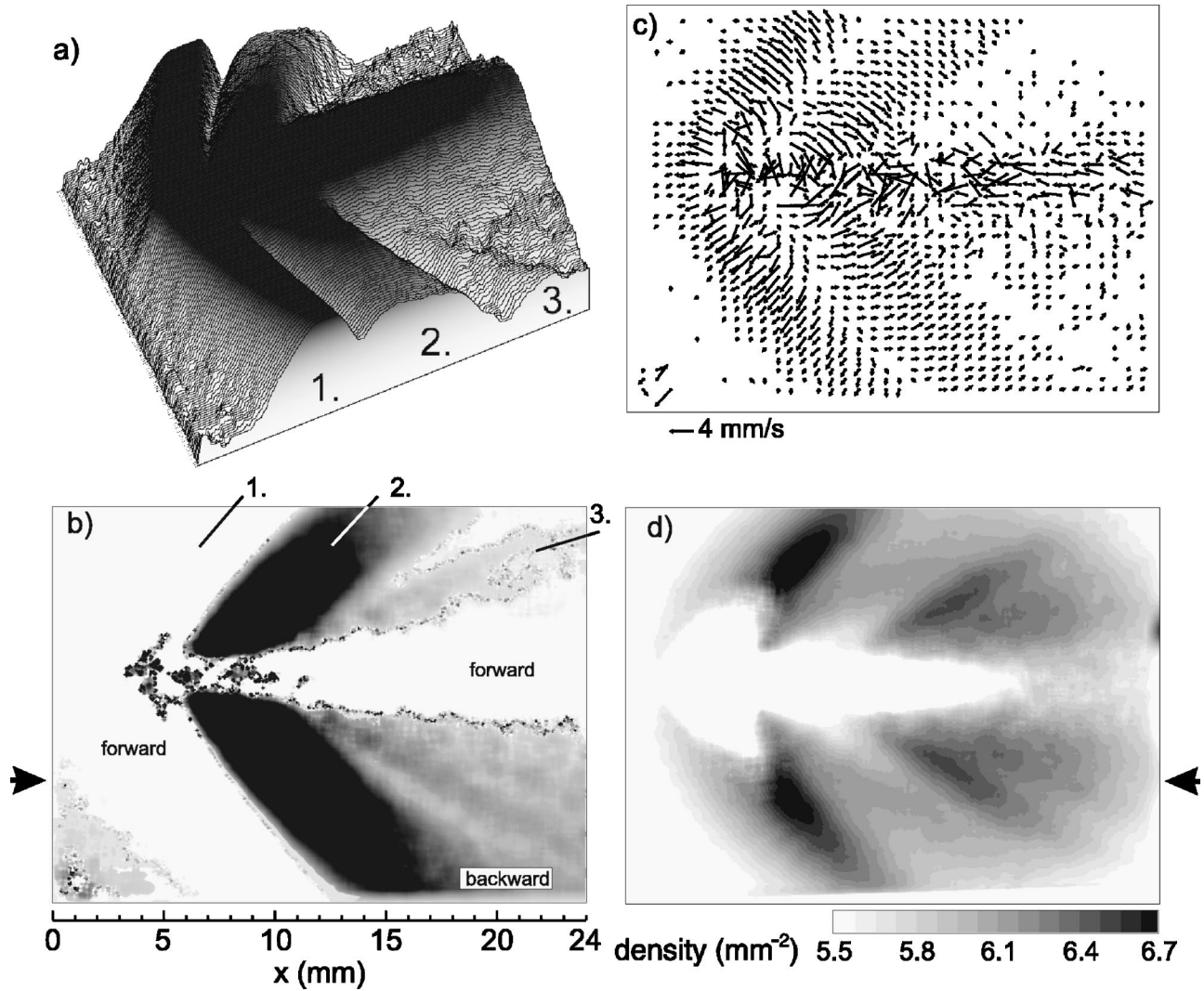
FIG. 7. Analysis of the Mach cone structure for the case of $V = 29.3$ mm/s (see Fig. 5). (a) Wire mesh representation of the speed map, (b) gray-scale coded particle velocity along the x direction, v_x (darker areas correspond to higher backward motion in the lab frame, white correponds to forward motion), (c) map of the particle velocity vectors $\vec{v}$, and (d) density map. The arrows indicate the line of the v_x and n_d profiles shown in Fig. 8.

B. Analysis of the Mach cone structure

Next we will discuss the structure of Mach cones. We will focus on a specific example, the Mach cone made with a laser spot velocity of 29.3 mm/s. In addition to the speed map shown in Fig. 5, we will present maps of additional physical quantities. All of these maps are based on data that were averaged over 100 scans.

First, we calculated maps for the velocity vector $\vec{v}$ as shown in Fig. 7(c). For clarity, we suppressed vectors shorter than 0.5 mm/s when drawing the map. Accompanying the vector plot of $\vec{v}$ is a gray-scale plot of the $\hat{x}$ component of $\vec{v}$, v_x, see Fig. 7(b). In this map, dark regions correspond to high velocity in the $+\hat{x}$ direction, which is opposite to the motion of the laser spot, whereas white corresponds to motion in the direction of the beam.

The map of number density n_d in Fig. 7(d) was prepared using the method of Ref. [21], which begins with a Wigner-Seitz (Voronoi) map of the lattice. The local number density is computed as the inverse of the area of the Wigner-Seitz cell for each particle, mapped onto a rectangular grid.

Additionally, we present cross-sectional slices along the x direction of the v_x map and the density map at the y position indicated by the arrows in Fig. 7. These slices are shown in Fig. 8.

One interesting feature is a long tail that is formed in the track of the laser spot. Within this track, particles move in the direction of the laser beam, as seen in Figs. 7(b) and 7(c). The number density of dust particles in this track is reduced, as shown in Fig. 7(d). This track is not observed in Mach cones generated by a moving charged particle [20,21]. We assume that this difference can be attributed to the difference in the forces acting on the particles in the track of the super-sonic object. As illustrated in Fig. 2, the laser spot, unlike a moving charged particle, imparts a net forward momentum to the particles. The resulting forward motion of the particles leaves a low-density track behind the spot. The track is then filled by particles moving in from outside the track, yielding a general backward drift motion behind the first cone. The track feature in the speed maps is rather long, an observation that in Sec. V we will attribute to the elongated shape of the
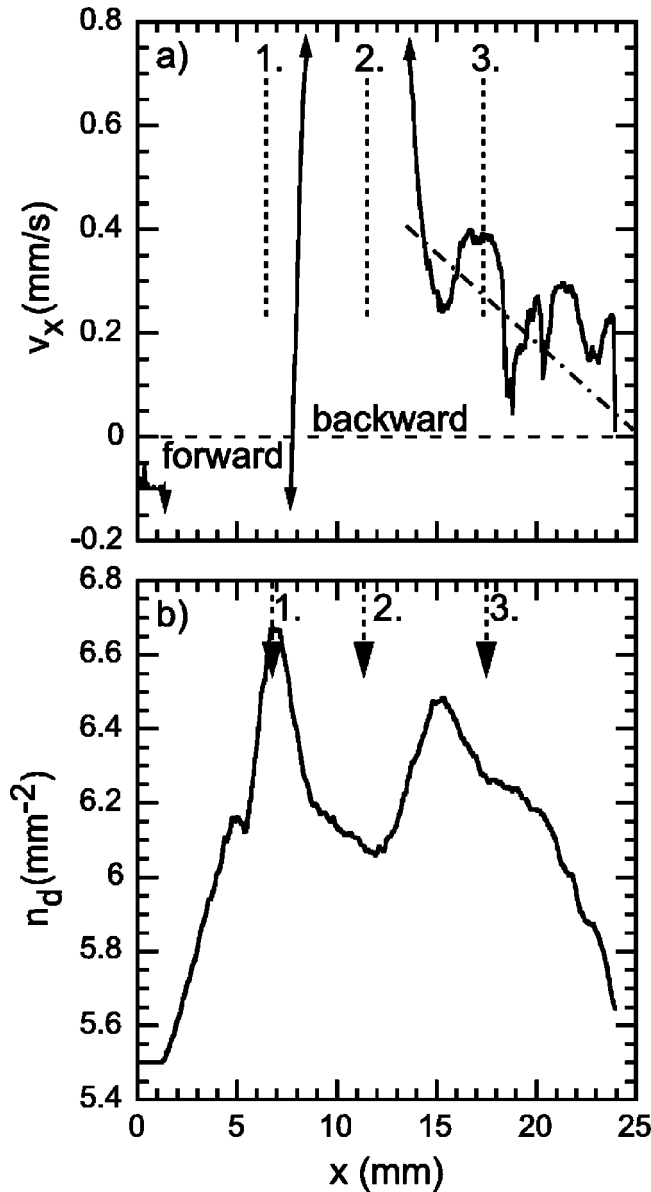
FIG. 8. Profiles of v_x (a) and n_d (b) along the x direction. The scale of v_x is expanded, clipping off the first and second cones, in order to bring out the third cone. The dashed vertical lines represent the location of maximum speed $|\vec{v}|$ of the first, second, and third cones, respectively. The inclined dash-dot line indicates a possible overall backward drift.

spot created by the tilted laser beam.

The speed map in Fig. 7(a) clearly shows the presence of a third peak, which we identified above as the third Mach cone. There is a reason, however, to question whether this feature might actually be the fourth cone, rather than the third. To consider this issue, we first examine the cross-sectional slice in Fig. 8. As expected, the first peak in number density coincides with the first cone of forward-moving particles, and the first minimum in density coincides with the second cone, with its backward-moving particles. Therefore, the first cone is compressional, while the second is rarefactional. These findings are consistent with the results for cones excited by a moving charged particle [20].

The third extremum in number density, however, does not coincide with the third peak in particle speed. Instead, the
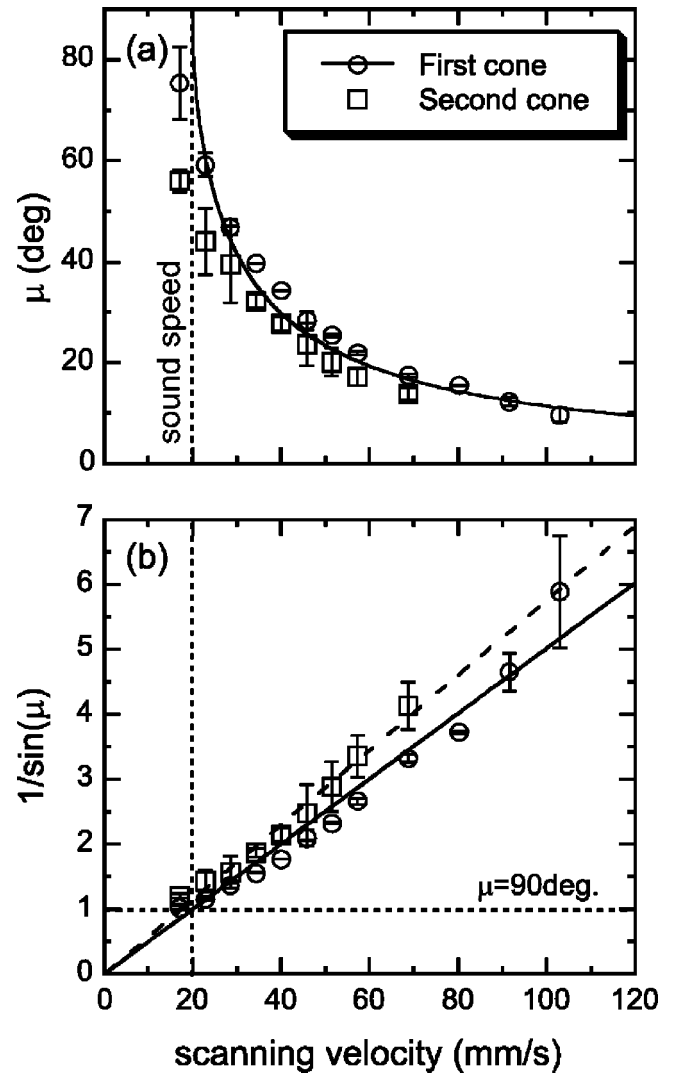

FIG. 9. (a) Mach cone angle μ of the first and second Mach cone measured from the speed maps as a function of the laser spot velocity V. (b) Plot of the Mach cone relation $1/\sin \mu = V/c$ for the first and second cone, respectively. From a linear fit, the sound speed c is found to be $c_1 = 19.9$ mm/s for the first cone and $c_2 = 17.4$ mm/s for the second. The sound speed c_1 is indicated as the vertical dashed line. In (a) the solid line for μ of the first cone is calculated using the sound speed c_1 derived from the linear fit in (b).

extremum in number density at $x = 15.5$ mm precedes the peak in particle speed at 17.5 mm. At the latter position, the number density does not have a profound peak or minimum, as would be expected. Moreover, the direction of particle motion at the third peak in the speed is backward in Fig. 7(b) and Fig. 8, rather than forward as predicted by earlier simulations for cones excited by a moving charged particle [20]. Thus, it is possible that the feature we have identified from the speed maps as the third cone might actually be the fourth cone.

It is possible that this discrepancy in counting cones arises from our using an absolute particle velocity, as measured in the lab frame. We have not adjusted the particle velocity for overall drifts in the particle motion produced by the laser beam. Outside the track behind the laser spot, the overall motion behind the first cone is backward, as can be seen in

Fig. 7(b) and Fig. 8. If this overall backward motion is merely a secular drift due to backfilling the track, then perhaps it should be subtracted out. To illustrate how this can be done, we have drawn an inclined dash-dot line in Fig. 8 to indicate the secular trend of v_x. Subtracting this trend from the measured velocity, the minimum in v_x at $x = 15.5$ mm becomes a *maximum in the forward direction*. This forward maximum velocity coincides, as one would expect, with a density maximum. If this explanation is correct, then the feature identified in Fig. 7(a) and 7(b) as the third cone is actually the fourth cone.

Finally, we evaluate the Mach cone as if it were a shock. Doing this, we quantify the strength of the shock from the jump in the density and pressure (normal stress, i.e., the diagonal elements of the stress tensor) from the undisturbed medium (with density n_1) to the peak in the first cone (with density n_2). The ratio of the densities is $n_2/n_1 = 6.7$ mm^2/5.5 mm$^2 = 1.2$, as determined from Fig. 8(b). Computing the ratio of the Coulombic pressure p_2/p_1 corresponding to these number densities, using the method of Samsonov *et al.* [21] and assuming a particle velocity $v = 4$ mm/s in the shock, we find that $p_2/p_1 \lesssim 1.5$, where the exact value depends on the particle charge and screening strength. With this pressure ratio the Mach shock can be classified as weak. For such a weak shock, it is possible that the particle motion might be nearly linear, rather than nonlinear.

C. Test of the Mach angle relation

Here we test the Mach angle relation Eq. (1) over a wider range of M and with less scatter than in the earlier test of Ref. [20]. This improvement was made possible by our use of the laser spot, which moved with a controlled speed and timing, where the latter allowed us to average many identical experimental runs to reduce the noise in our images. We covered the range $10° < \mu \leqslant 80°$, which is a wider range, especially close to $M = 1$, than in a previous experiment [21]. We measured the cone angles manually, using the speed maps in Fig. 5. The cone angles of the first and second Mach cone are shown in Fig. 9(a) for the conditions of experiment VI.

The Mach angle relation Eq. (1) is tested in Fig. 9(b). This is a plot of $1/\sin \mu$ versus V. The points for the first and the second cone fall on separate straight lines, indicating the validity of the Mach angle relation. From a linear fit of Mach number, the sound speed for the first and second cone are found, as listed in Table I. For the experimental conditions VI that were used for Fig. 9, we find $c_1 = 19.9$ mm/s and $c_2 = 17.4$ mm/s.

There are three physics conclusions we can draw from the data shown in Fig. 9(b). First, the quality of the fit to straight lines in Fig. 9(b) is evident, verifying that the Mach angle relation is applicable when a dusty plasma is disturbed by a supersonic disturbance. Second, the ≈ 20 mm/s speed of the wave is quite slow, due to the low charge-to-mass ratio of the particles in a dusty plasma. Third, the two cones have different angles, indicating that the second cone ''sees'' a slower sound speed than the first.

The reason for the slower sound speed in the second cone is not clear. One possibility is that nonlinear effects might be
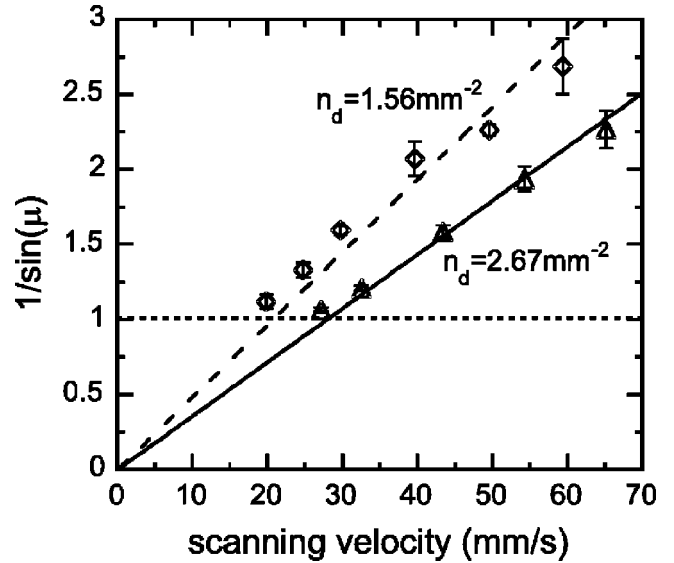

FIG. 10. Sound speed dependence on number density. The solid and broken curves are for experimental conditions I and II, respectively, which are for two different regions of the same lattice in the same discharge. A higher number density corresponds to a higher sound speed.

involved, if the sound speed of the second cone is reduced due to a diminished number density behind the first cone. Determining whether nonlinearity is the cause will require further study in simulations and experiments, where the strength of the laser excitation can be varied.

The possibility that the first and second cone correspond to the compressional and shear waves, respectively, can be ruled out two ways. First, we have observed more than two cones. Second, the sound speed for the second cone is too close to that of the first cone. In the experiment, $c_1/c_2 = 1.14$, whereas the theory of Peeters and Wu [18] predicts that the compressional wave is five times faster than the shear wave, for $\kappa = 1$.

A useful test of the dependence of the sound speed c on the particle number density is shown in Fig. 10. Here, the Mach cones have been excited under the same discharge conditions, but in different parts of the crystal cloud, in the center and at the edge. As mentioned in the Introduction, the number density is highest in the center and lower at the edge, corresponding, for example, to experimental conditions I and II, respectively. While the number density varies from the center to the edge of the particle cloud, we believe the plasma conditions and therefore the charge do not. That is because the plasma is produced by the electrode, which has a much larger diameter than the suspension of microspheres. From Fig. 10 it is seen that at a higher number density, the sound speed is faster. This is expected, since the spring constant increases when the crystal is more compressed. This tendency is quantified in Eq. (3). We will exploit our ability to measure sound speeds at two different number densities in the next section, yielding a measurement of the screening strength and, consequently, the particle charge.

IV. METHODS OF MEASURING Q AND κ FROM THE SOUND SPEED

The particle charge Q and the screening strength κ are crucial parameters in the determination of the crystal prop-

erties. Various methods have been developed to measure them, which we review next. Then, we will present several new methods that we have devised, based on the sound speed measured from Mach cones.

A. Review of previous methods

The first method was the resonance technique [6,26], which is based on the force equilibrium between electric field force and gravity. Particles are shaken in the vertical direction by modulating the voltage on the lower electrode. The vertical resonance frequency can be measured with high precision. The method also requires a value for the ion density in the sheath, which must be extrapolated from Langmuir-probe measurements made in the bulk plasma region. The method assumes that the electric potential profile in the sheath is parabolic.

As a second method, binary collisions were used by Konopka *et al.* to measure both Q and κ [27,9]. This method is limited to use with a suspension of two particles that can be made to collide. The parameters are determined by fitting the particle orbits in a center-of-mass frame.

A third method involves comparing experimentally measured and theoretical DLW dispersion relations to provide a measurement of κ. The first authors to use this method [12,13] employed the resonance method to measure Q. In recent experiments with a linear chain [28] both Q and κ were measured simultaneously by fitting the dispersion of the DLW. These methods use a dispersion relation that assumes a Yukawa interparticle potential.

Fourth, the dust charge Q was determined in previous experiments with Mach cones [20,21] by measuring the sound speed from the cone angle and comparing to the sound speed predicted by the theoretical dispersion relation for a 2D DLW assuming a Yukawa potential. In the theory, the authors included nearest-neighbor [20] and second-nearest-neighbor [21] interactions, which we will discuss below. Their method required an independent measurement of κ. As usual, direct measurements of the particle spacing a are very precise while those of the Debye length are not, due to the inaccuracies of Langmuir probes and the fact that they can only be used in the bulk plasma rather than at the height of the particle layer. The same limitation applies to the resonance method. These authors measured the ion Debye length λ_D with a Langmuir probe in the bulk plasma, and extrapolated the measurement to the sheath using an arbitrary multiple to reduce the density. This extrapolation scales only with the square root of the ion density, which is weaker than the scaling in the resonance technique, giving rise to a smaller error.

Except for the collision method, all of these *in situ* techniques for measuring Q and/or κ rely on extrapolating Langmuir-probe measurements of the bulk plasma properties into the sheath. Therefore, they are subject to a certain degree of error. Here we develop methods intended to circumvent these problems.

Below, we will present two different methods to determine Q and κ using the sound speed measured from Mach cones. The first method is based on the difference in sound speed for different dust number densities under the same plasma conditions (see Fig. 10). The second uses the sound
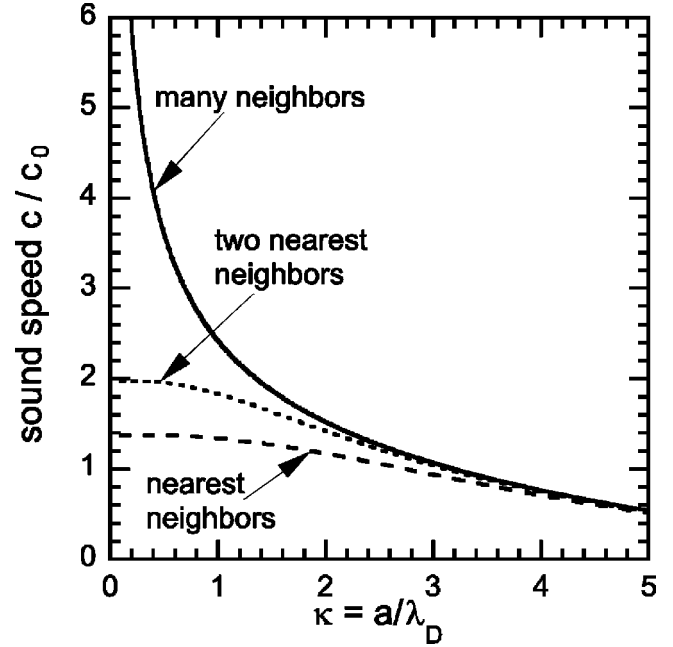

FIG. 11. Theoretical determination of the normalized sound speed $c/c_0=f(\kappa)$ as a function of the screening strength κ. The sound speed is shown for the exact solution (solid line) and by taking into account nearest neighbors and two nearest neighbors (dashed lines).

speed and the vertical resonance frequency. An advantage of these methods is that neither relies on an absolute measurement of the ion density in the sheath. They both use a sound speed predicted by a theoretical dispersion relation that assumes a Yukawa potential. We will review this theory next.

B. Sound speed theory

The sound speed of a compressional wave in a 2D Yukawa system depends on the screening strength κ, as in Eq. (2). This dependence is plotted in Fig. 11, where in calculating the sum in $f(\kappa)=c/c_0$ we included various numbers of neighbors. The most accurate expression includes many neighbors, which we define to be a number large enough to assure that $r_{a,max}\kappa\gg1$. For large κ, it is adequate to retain only one or two nearest neighbors in the sum. However, the error becomes significant if one includes only one ring ($r_a=1$) or two rings of neighbors, for $\kappa\lesssim1.5$ and $\kappa\lesssim1$, respectively. In previous Mach cone experiments [21] where $\kappa\gtrsim1.5$, it was justified to include only one or two rings. Here, however, we will include many neighbors, $r_{a,max}\kappa\gg1$.

The two methods of measurement described below differ in the input parameters that are used. Most importantly, they differ in the way that κ is measured. Both methods use as an input parameter the measured sound speed, and they both assume that the sound speed is accurately predicted by the dispersion relation for a 2D Yukawa lattice.

C. Sound-speed ratio method of measuring κ and Q

Here, we present a method where the screening strength κ is determined by measuring the sound speed for different particle number densities, under otherwise identical plasma conditions. The experimental data we use are shown in Fig.
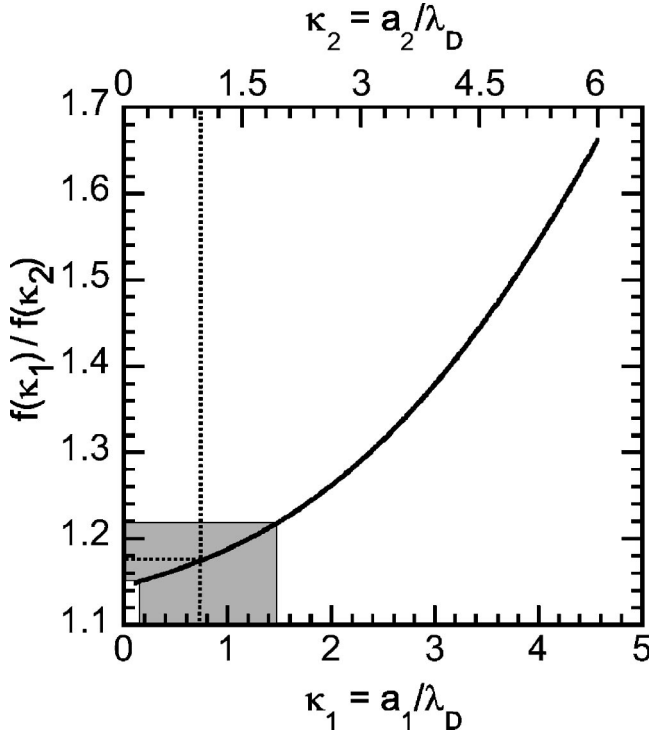
FIG. 12. Plot of $f(\kappa_1)/f(\kappa_2)$ as a function of κ_1. The horizontal dashed line indicates the experimental value $f(\kappa_1)/f(\kappa_2)=1.18$. See text for details.

10. There, the sound speed c_1 and c_2 were measured in two different regions of the same plasma crystal, with interparticle distances a_1 and a_2, respectively. These two conditions are identified in Table I as experiments I and II.

We assume that the particle charge is the same in the two parts of the plasma crystal. This assumption is justified because the measurements were performed under the same plasma conditions. The relevant plasma conditions for determining the charge are the electron temperature, ion drift speed, and the electron/ion density ratio at the height of the lattice. These plasma conditions likely do have radial gradients, but we expect them to be on the scale of the electrode radius, which was much larger than the particle cloud diameter. Therefore, it is reasonable to assume that the plasma conditions and therefore the charge were uniform throughout the cloud.

When the charge is the same, we can compute κ from the ratio of the sound speeds c_1/c_2 and the interparticle distance. This can be expressed as

$$\frac{f(\kappa_1)}{f(\kappa_2)} = \frac{c_1}{c_2}\frac{\sqrt{a_1}}{\sqrt{a_2}},$$

where $\kappa_{1,2} \equiv a_{1,2}/\lambda_D$. The dependence of $f(\kappa_1)/f(\kappa_2)$ on κ_1 and κ_2 is plotted in Fig. 12. By computing the quantity on the horizontal axis, $c_1\sqrt{a_1}/c_2\sqrt{a_2}=1.18$ from the measured values, one obtains the values of κ_1 and κ_2. This is our first method of measuring κ.

We now demonstrate this method with our data, computing κ and then Q. For our experiment, this method yields $\kappa_1=0.70$ and $\kappa_2=0.92$. Using this, along with the measured value of the sound speed c in Eq. (2) and Eq. (3), yields the

charge Q. We find that $Q=7000e$. This value is, of course, assumed to be the same for both regions of the crystal.

There is a significant uncertainty in the measured value of κ due to the small slope of the curve in Fig. 12. For the parameter range of greatest interest, $\kappa < 2$, the slope is smallest. Although the measured sound speed has a small error, this error is magnified by the small slope. For our experiment, we find an error in κ of ± 0.7, which unfortunately is comparable to the value itself.

Overcoming this difficulty might require measuring c with a smaller error than in our present experiment. We used a manual method of measuring the Mach angle from the speed maps. Perhaps this method could be improved by some kind of numerical fitting routine based on the image data, or it could be replaced by exciting compressional waves in some form other than Mach cones.

Offsetting this difficulty is the advantage of this method: it does not rely on any probe measurements. It relies instead on c and a, which are parameters measured from particle images. Particle positions and quantities computed from them are generally much more precise than probe measurements. Moreover, probes cannot be used in the sheath, where the particles are levitated. The primary assumptions of this method are the dispersion relation of the compressional waves in the crystal lattice and the assumption that the interparticle potential is Yukawa.

D. Combined sound-speed and resonance method of measuring κ and Q using a probe

Here, a second method is developed that combines features of two earlier methods, the resonance technique [6,26] and Mach cones [20,21]. This combined method relies on measurements of the sound speed, the interparticle distance, and the vertical resonance frequency ω_0. In the original method by Samsonov et al. [20,21], the Debye length is used as a parameter that enters the calculation of the dust charge Q. Since the electron and ion densities n_e and n_i at the crystal position in the sheath are not known very accurately, the Debye length itself is not very precise. In our combined method, the dust charge is restricted by the additional measurement of the vertical resonance frequency [6,26]. This allows us to replace two imprecise input parameters, n_i and n_e, by one that is precise, the vertical resonance frequency ω_0, and one that is not, the electron-to-ion density ratio $\alpha \equiv n_e/n_i$.

The combined method makes use of the following relations:

$$c = \sqrt{\frac{Q^2}{4\pi\epsilon_0 ma}}f(a/\lambda_D), \tag{4}$$

$$\lambda_D^{-2} = \frac{n_i e^2}{\epsilon_0 kT_e} + \frac{n_e e^2}{\epsilon_0 kT_e} = \frac{n_i(1+\alpha)e^2}{\epsilon_0 kT_e}, \tag{5}$$

$$Q = \sqrt{\frac{\epsilon_0 m}{n_i(1-\alpha)e}}\omega_0. \tag{6}$$

This set of equations has the desirable feature that they can be combined to eliminate variables such as n_i that cannot be measured accurately at the height of the particles. Equa-
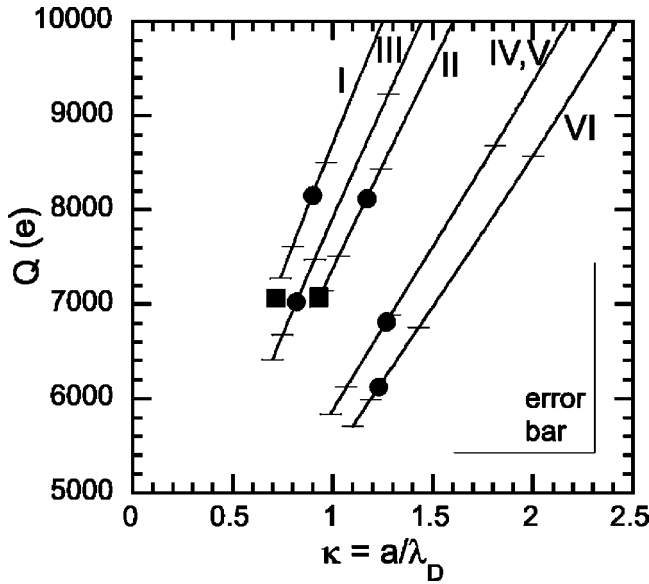
FIG. 13. Summary of the experimental results in the Q, κ plane. The solid lines indicate the values of Q and κ compatible with the experimental values of the sound speed, interparticle distance, vertical resonance frequency, and electron temperature with the electron-to-ion density ratio α as free parameter, based on the method of Sec. IV D using Eqs. (4)–(6). The tick marks indicate the values corresponding to $\alpha = 0, 0.1, 0.33, 0.66$ from bottom to top. The solid squares indicate κ (and thus Q) obtained using the sound-speed ratio method of Sec. IV C. The circles are κ and Q obtained in a method similar to Ref. [21]. The roman numerals I–VI indicate the experiment number as listed in Table I.

tion (4) is the sound-speed relation, which assumes the dispersion relation for a 2D Yukawa lattice. Equation (5) defines the Debye length, and this relation requires some explanation. Because the particles are levitated slightly within the sheath, where the ions have been accelerated to an energy on the order of kT_e, we have assumed, in the denominator of the second term of Eq. (5), that the appropriate energy for the screening by ions is kT_e. This assumption is supported by previous experimental findings [9,12,13,27]. The electron temperature T_e is determined experimentally from Langmuir probe measurements in the bulk plasma, at a height above the particle layer. Unlike n_i, this parameter is believed to have nearly the same value in the bulk plasma as in the sheath. Equation (6) imposes a restriction on the dust charge or equivalently the ion density at the crystal position by the measured vertical resonance frequency ω_0 according to the resonance technique [6,26]. In addition to T_e, this method uses as inputs the values of c, a, and ω_0, which are all measured precisely from particle images.

In Fig. 13, the lines in Q, κ phase space represent the sound-speed relation according to Eq. (2) or (4) using the measured values of c and a for experimental conditions I–VI, thus each pair of Q, κ on the line results in the measured sound speed c. Both methods presented here (the sound-speed ratio and the combined method) make use of the sound speed, and either the determination of Q or κ fixes a point on this line.

From the combined method one can parametrize the sound-speed relation by the single parameter α using Eqs. (5) and (6) to eliminate the ion density n_i. The thin tick

marks on the solid curves indicate the values $\alpha = 0, 0.1, 0.33, 0.66$, beginning from the bottom. In doing so, a minimum value for Q and κ is identified. Thus, the bottom end of these curves corresponds to the minimum value of $\alpha = 0$, which would apply if there were no electrons present at the height of the crystal. Fortunately, we find that Q and κ are not extremely sensitive to α. As seen in Fig. 13, κ and Q vary typically over a range of $\pm 30\%$ and $\pm 20\%$, respectively, for $0 \leq \alpha \leq 0.66$.

Our experiment was performed with a radio-frequency sheath. During the rf cycle, the sheath repeatedly expands and then collapses, and during its collapse the electron-rich plasma extends all the way to the electrode. The densities and electric potential have both dc and time-varying rf components. The particles, like the ions, are so massive that they respond only to the dc potential. Therefore, it is the time-averaged densities n_i and n_e that enter into $\alpha \equiv n_e / n_i$. This ratio is nonzero since the rf sheath, unlike a dc sheath, has a finite electron density penetrating to the electrode during the sheath collapse.

E. Comparison of methods of measuring κ and Q from Mach cones

Here we compare the two methods of measuring Q, κ described above. Data points from the sound-speed ratio method of Sec. IV C are shown as squares in Fig. 13. Comparing the two, we find that the data for the sound-speed ratio method fall very nearly at the bottom end of the curves for the combined method of Sec. IV D. The bottom of those curves corresponds to $\alpha = 0$.

We also compare to the method of Ref. [21], which also used the sound speed measured from the Mach angle. In that method, κ is determined by measuring the Debye length with Langmuir probes in the bulk plasma. The Debye length is adjusted upward by an arbitrary factor, corresponding to a reduction in the ion density, in the sheath as compared to where the probe measurement was made. Here we must choose the ion density reduction arbitarily, in our case by a factor of 5. The corresponding increase in the Debye length is a factor of $\sqrt{5}$. This adjustment is accurate within 50%, for ion density reductions in the sheath by a factor between 2 and 20.

Typical error bars for determining κ and Q are indicated in the figure. For the sound-speed ratio method, the error for κ is ± 0.7 due to the small slope of $f(\kappa_1)/f(\kappa_2)$ in Fig. 12, as explained in Sec. IV C. The error bar for κ also reflects the above-mentioned 50% uncertainty in the extrapolation of the shielding length into the sheath. These errors in determining κ give rise to the indicated error range for the particle charge Q.

For both the sound-speed ratio method and the method of Ref. [21], the data fall on the curves for the combined method in a range $0.1 \leq \alpha \leq 0.33$. If all the methods are correct, this result suggests that the electron density is greatly reduced as compared to the ion density, at the height where the particles are levitated. In this case, the interparticle shielding would likely be provided mainly by ions rather than electrons.

V. MOLECULAR-DYNAMICS SIMULATIONS

We carried out molecular-dynamics (MD) simulations, re-producing the experiment as faithfully as was practical. The particle equation of motion,

$$m\frac{d^2\vec{r}}{dt^2} = -Q\nabla\phi - \nu\frac{d\vec{r}}{dt} + F_L, \qquad (7)$$

was integrated for $N=5000$ particles. The electric potential was

$$\phi = -\frac{k}{2}r^2 - \sum_{i<j}^{N}\frac{Q}{4\pi\epsilon_0 r_{ij}}\exp\left(-\frac{r_{ij}}{\lambda_D}\right), \qquad (8)$$

where the first term is a harmonic potential for the radial confinement and the second term is a binary interparticle repulsion, assuming a Yukawa model. Here r is the distance from the axis, r_{ij} is the distance between any two particles, and the sum is over all particles.

We used the parameters $Q=6860e$, $\lambda_D=330$ μm, $m=2.18\times10^{-13}$ kg, and $\nu=2.3$ s^{-1} for Epstein drag. These parameters are like those for experiment V in Table I, Fig. 5, and Fig. 6. We chose $k=5.46\times10^{-13}$ kg/s^2 to achieve a particle separation $a=420$ μm, corresponding to $\kappa=1.27$, when averaged over the region shown in the figures.

The simulation ran as follows. Particles were seeded with random initial positions. Then, while integrating Eq. (7), particles moved about. Eventually they settled into equilibrium positions, with their kinetic energy lost entirely to damping. We then introduced a moving localized force F_L to model the force due to the moving laser spot. As in Fig. 2, the force was modeled with an elliptical Gaussian profile, $F_L=-f_0\exp[-(x-Vt)^2/b_x^2]\exp(-y^2/b_y^2)\hat{x}$. To make it similar to the experiment, the elongated laser footprint had the parameters $b_y=0.33$ mm and $b_x=b_y/\sin\theta=1.9$ mm with $\theta=10°$. The laser spot velocity was $V=29.3$ mm/s, as in one of the experiments in Fig. 5.

The force at the center of the beam was $f_0=2.2\times10^{-14}$ N. We chose this value empirically to yield approximately the same particle velocity as in Fig. 7 for the experiment. This force is equivalent to $0.01mg$, in terms of the gravitational acceleration g.

The speed map from the simulation, Fig. 14, shows general agreement with the experiment. In both the simulation and the experiment, the first and second cones are prominent, and a third cone is faintly visible.

The experiment and simulation yielded generally comparable values for the angles of the first and second cones, but there is a discrepancy. Our measurements, made from the speed maps with an accuracy of typically $\pm1.5°$, were as follows. In the simulation, the first two cones have an angle $\mu_1=49.5°$ and $\mu_2=44.5°$. In the experiment, $\mu_1=53°$ and $\mu_2=41.5°$. The angles in the experiment and the simulation are generally comparable. Nevertheless, there is a discrepancy in the difference of the first and second cone angles. The difference $\mu_1-\mu_2=5°$ is much smaller than the $11.5°$ difference for the experiment. We do not know the reason for this discrepancy, or whether it could be resolved by choosing different simulation parameters.
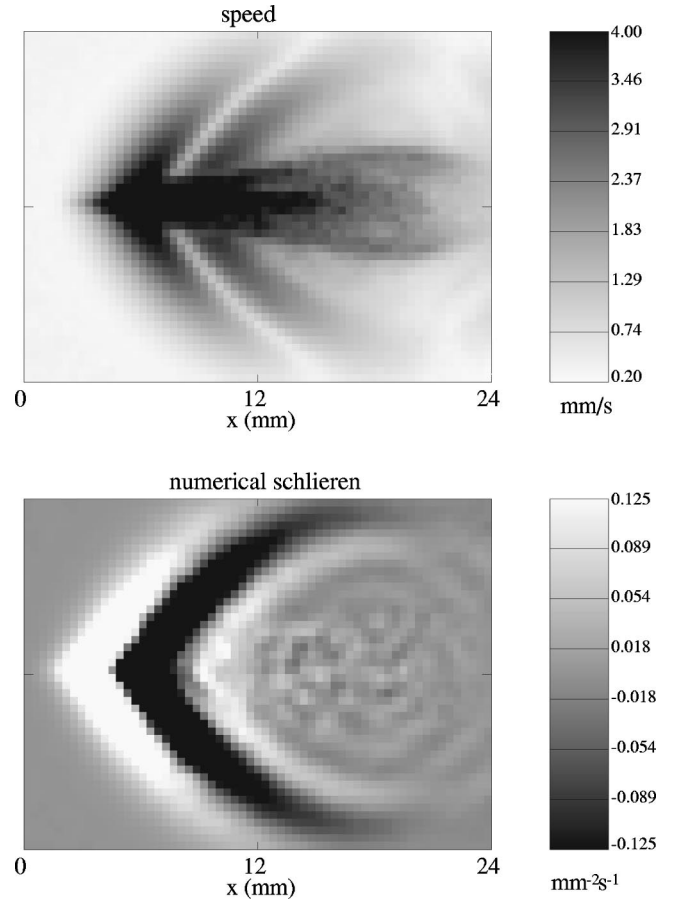

FIG. 14. From the MD simulation, a gray-scale map of the particle speed $|\vec{v}|$ and a Schlieren map, both for $V=29.3$ mm/s. Unlike the experiment where the Schlieren map is produced from an uncalibrated video image of particles, here it is computed from the number density, and therefore a calibration scale is shown. These plots should be compared to the experimental data in Figs. 5 and 6.

The numerical Schlieren map was computed in a way analogous to the experimental map. The difference is that the experimental map was prepared from the video image of particles, while in the simulation we used the number density directly. The quantity we plot here is the difference $n_d(x,y,t)-n_d(x,y,t-1/30$ sec$)$. Because of the different methods of preparation, one might not expect the numerical Schlieren maps for the experiment and simulation to look exactly alike.

The numerical Schlieren map from the simulation, Fig. 14, also shows the Mach cones. The first two cones, as in the speed maps, are more nearly equal in angle in the simulation than in the experiment. Indeed, in the simulation, the second cone is nested directly against the first cone.

We also note in the numerical Schlieren map from the simulation that there appear to be some random compressional disturbances in the track behind the laser spot. If our medium were a continuum, rather than discrete particles, one might be tempted to describe these disturbances as "acoustic turbulence."

Now we will use the simulation to explain the experimental observation of an elongated low-density region in the track behind the moving laser spot. To do this, we repeated
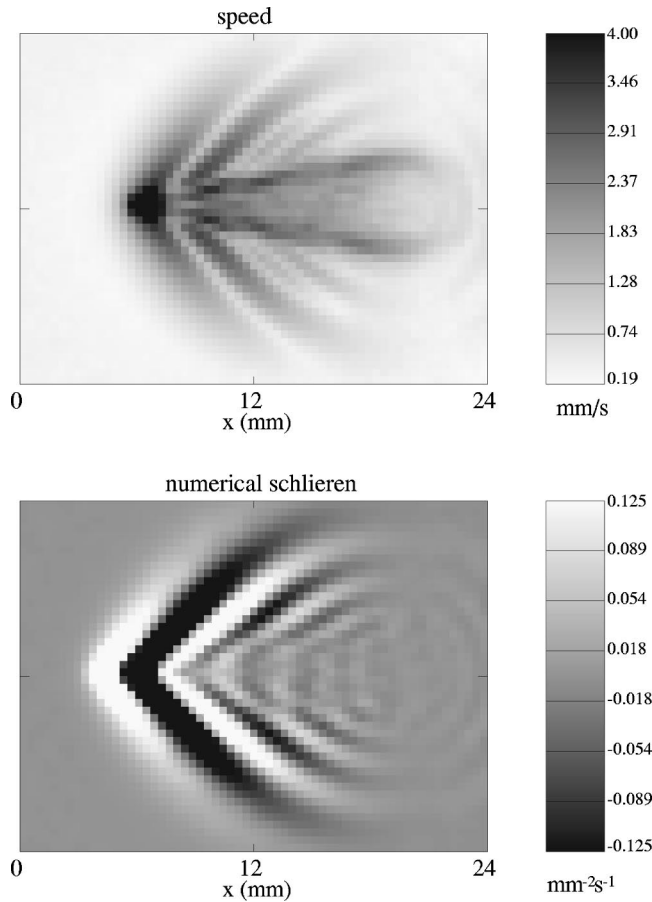
FIG. 15. From the MD simulation, with a laser spot that has been artificially reshaped so that it makes a round footprint on the lattice. Otherwise, this is like Fig. 14. Comparing these two figures reveals the effects of an elongated laser footprint.

the simulation with a laser footprint that was round, with $b_x = b_y = 0.33$ mm, rather than elliptical. Diffraction limiting would prevent one from shaping a narrow laser beam this way in the experiment, so this test can only be done in the simulation. To achieve approximately the same peak particle speed as before, we increased f_0 by 50%. Nevertheless, the momentum applied to the crystal as a whole was reduced by a factor 0.26, because the shorter laser footprint resulted in a smaller value of $\int F_L dx$.

The resulting simulation results for a circular laser beam footprint, shown in Fig. 15, lead us to two conclusions. First, we note that the high-speed region in the track behind the laser footprint becomes shorter when the laser footprint is shortened into a round spot. This verifies our earlier explanation that the elongated track in the experiment is due to the elongated laser beam. Second, we observe in the simulation that the third cone becomes clearer and additional cones appear when the footprint becomes round. This suggests that in our experiment, the elongated laser footprint causes the third- and higher-order cones to overlap and obscure one another.

VI. SUMMARY

We have performed experiments on Mach cones in single-layer plasma crystals. We have shown that the Mach cones can be excited by sweeping a focused laser beam with a supersonic velocity through the plasma crystal. The use of a laser generates repeatable Mach cones over a large range of subsonic and supersonic speeds. This was done in a controlled manner, allowing a large number of repetitions of an experiment. Averaging these repetitions allowed us to identify a number of features that would otherwise be obscured by noise.

We have demonstrated the existence of a third Mach cone and possibly a fourth cone as well. This multiple cone structure was anticipated in earlier simulations [20], and it rules out the possibility that the cone structure with two cones, observed in earlier experiments [20], was generated by the two possible wave modes in a plasma crystal. The Mach cone relation has been verified with quite high accuracy over a large range of supersonic velocities. It is found that for increasing order of the Mach cones, the cone angles become smaller and thus the corresponding sound velocity decreases slightly.

In an experiment performed in different crystal regions with different dust density, but at the same plasma conditions, it was demonstrated that the sound speed c increases with dust density. This finding was used to devise an *in situ* method for measuring the screening strength κ (and, therefore, the dust charge Q) in the plasma crystal. This method does not depend on any knowledge of the plasma parameters at the crystal position.

A second technique was developed for measuring the dust charge and screening strength that replaces some of the unknown parameters, such as electron and ion density at the crystal position, by other more accurately measurable quantities. From these measurements the screening strength is found to be in the range $\kappa = 0.5-1.3$ and the corresponding dust charge is $Q = 6000-8000$ elementary charges, depending on the discharge conditions.

Finally, we have performed MD simulations of the Mach cones in a plasma crystal using the experimental conditions. The simulation, which assumed a Yukawa potential, yielded results that were generally comparable to the experiment. The simulation helped us explain the experimentally observed long track behind the laser spot. This track, which results from the net momentum imparted on the particles by the laser beam, had a considerable length in the experiment due to the shape of the laser spot that excited the Mach cones.

[1] O. Havnes *et al.*, J. Geophys. Res. [Space Phys.] **100**, 1731 (1995).

[2] H. Thomas *et al.*, Phys. Rev. Lett. **73**, 652 (1994).

[3] Y. Hayashi and K. Tachibana, Jpn. J. Appl. Phys., Part 2 **33**, L804 (1994).

[4] J. Chu and Lin I, Physica A **205**, 183 (1994).

[5] J. Chu and Lin I, Phys. Rev. Lett. **72**, 4009 (1994).

[6] A. Melzer, T. Trottenberg, and A. Piel, Phys. Lett. A **191**, 301 (1994).

[7] A. Melzer, A. Homann, and A. Piel, Phys. Rev. E **53**, 2757 (1996).

[8] H. Thomas and G. E. Morfill, Nature (London) **379**, 806 (1996).

[9] U. Konopka, G. Morfill, and L. Ratke, Phys. Rev. Lett. **84**, 891 (2000).

[10] F. Melandsø and J. Goree, Phys. Rev. E **52**, 5312 (1995).

[11] A. Melzer, V. Schweigert, and A. Piel, Phys. Rev. Lett. **83**, 3194 (1999).

[12] A. Homann, A. Melzer, S. Peters, and A. Piel, Phys. Rev. E **56**, 7138 (1997).

[13] A. Homann, A. Melzer, R. Madani, and A. Piel, Phys. Lett. A **173**, 242 (1998).

[14] O. Havnes *et al.*, J. Vac. Sci. Technol. A **14**, 525 (1996).

[15] J. Bond, K. Watson, and J. Welch, *Atomic Theory of Gas Dynamics* (Addison-Wesley, Reading, MA, 1965).

[16] N. Cheng, Z. Zhu, C. Cheng, and M. Toksöz, Geophys. Prospect. **42**, 303 (1994).

[17] G. Crapper, *Introduction to Water Waves* (E. Harwood, Chichester, England, 1984).

[18] F. Peeters and X. Wu, Phys. Rev. A **35**, 3109 (1987).

[19] F. Melandsø, Phys. Plasmas **3**, 3890 (1996).

[20] D. Samsonov *et al.*, Phys. Rev. Lett. **83**, 3649 (1999).

[21] D. Samsonov, J. Goree, H. M. Thomas, and G. E. Morfill, Phys. Rev. E (to be published).

[22] V. A. Schweigert and F. Peeters, Phys. Rev. B **51**, 7700 (1995).

[23] Y. Lai and Lin I, Phys. Rev. E **60**, 4743 (1999).

[24] A. Melzer *et al.*, Phys. Rev. E **54**, 46 (1996).

[25] V. A. Schweigert *et al.*, Phys. Rev. E **54**, 4155 (1996).

[26] T. Trottenberg, A. Melzer, and A. Piel, Plasma Sources Sci. Technol. **4**, 450 (1995).

[27] U. Konopka, L. Ratke, and H. M. Thomas, Phys. Rev. Lett. **79**, 1269 (1997).

[28] H. Schollmeyer, A. Melzer, A. Homann, and A. Piel, Phys. Plasmas **6**, 2693 (1999).